

Long-range magnetic order in real icosahedral quasicrystals

Ryuji Tamura (✉ tamura@rs.tus.ac.jp)

Tokyo University of Science <https://orcid.org/0000-0001-8589-4311>

Asuka Ishikawa

Tokyo University of Science

Shintaro Suzuki

Tokyo University of Science

Akihiro Kotajima

Tokyo University of Science

Yujiro Tanaka

Tokyo University of Science

Takehito Seki

University of Tokyo

Naoya Shibata

University of Tokyo <https://orcid.org/0000-0003-3548-5952>

Tsunetomo Yamada

Tokyo University of Science <https://orcid.org/0000-0003-0138-9778>

Takenori Fujii

The University of Tokyo

Chin-Wei Wang

National Synchrotron Radiation Research Center <https://orcid.org/0000-0001-9012-2420>

Maxim Avdeev

Australian Nuclear Science and Technology Organisation, Australia

Taku Sato

Tohoku University

Article

Keywords: Quasicrystals (QCs), long-range magnetic order, icosahedral symmetry

Posted Date: March 23rd, 2021

DOI: <https://doi.org/10.21203/rs.3.rs-215127/v1>

License:  This work is licensed under a Creative Commons Attribution 4.0 International License.

[Read Full License](#)

1 **Long-range magnetic order in real icosahedral quasicrystals**

2

3 Ryuji Tamura^{1*}, Asuka Ishikawa², Shintaro Suzuki¹, Akihiro Kotajima¹, Yujiro Tanaka¹,
4 Takehito Seki³, Naoya Shibata³, Tsunetomo Yamada⁴, Takenori Fujii⁵, Chin-Wei Wang⁶,
5 Maxim Avdeev^{7,8} and Taku J. Sato^{9*}

6

7 ¹Department of Materials Science and Technology, Tokyo University of Science,
8 Katsushika, Tokyo 125-8585, Japan,

9 ²Research Institute for Science and Technology, Tokyo University of Science, Katsushika,
10 Tokyo 125-8585, Japan,

11 ³Institute of Engineering Innovation, School of Engineering, The University of Tokyo,
12 Bunkyo, Tokyo 113-8656, Japan,

13 ⁴Department of Applied Physics, Tokyo University of Science, Katsushika, Tokyo 125-
14 8585, Japan,

15 ⁵Cryogenic Research Center, The University of Tokyo, Bunkyo, Tokyo 113-0032, Japan,

16 ⁶National Synchrotron Radiation Research Center, Hsinchu 30076, Taiwan,

17 ⁷Australian Nuclear Science and Technology Organisation, New Illawarra Road, Lucas
18 Heights, NSW 2234, Australia,

19 ⁸ School of Chemistry, The University of Sydney, Sydney, NSW 2006, Australia,

20 ⁹Institute of Multidisciplinary Research for Advanced Materials, Tohoku University, 2-1-
21 1 Katahira, Aoba, Sendai 980-8577, Japan

22 *e-mail: tamura@rs.tus.ac.jp; taku@tohoku.ac.jp

23 **Abstract**

24 **Quasicrystals (QCs), first discovered in 1984¹, generally do not exhibit long-range**
25 **magnetic order. Here, we report on long-range magnetic order in the real**
26 **icosahedral quasicrystals (*i* QCs) Au–Ga–Gd and Au–Ga–Tb. The Au₆₅Ga₂₀Gd₁₅ *i***
27 **QC exhibits a ferromagnetic transition at $T_C = 23$ K, manifested as a sharp anomaly**
28 **in both magnetic-susceptibility and specific-heat measurements. Quick magnetic**
29 **saturation to almost the full moment ($7\mu_B/\text{Gd}^{3+}$) is observed under 100 Oe at 2 K.**
30 **This is the first observation of long-range magnetic order in a real quasicrystal, in**
31 **contrast to the spin-glass-like behaviours observed for the other magnetic**
32 **quasicrystals found to date. Moreover, when Gd is replaced by Tb, i.e. for the**
33 **Au₆₅Ga₂₀Tb₁₅ *i* QC, a ferromagnetic behaviour is still retained with $T_C = 16$ K.**
34 **Although the sharp anomaly in the specific heat observed for the Au₆₅Ga₂₀Gd₁₅ *i* QC**
35 **is significantly broadened upon Tb substitution, neutron-diffraction experiments**
36 **clearly show the marked development of magnetic Bragg peaks below T_C , indicating**
37 **long-range magnetic order for the Au₆₅Ga₂₀Tb₁₅ *i* QC also. Our findings can**
38 **contribute to the further investigation of exotic magnetic orders formed on real**
39 **quasiperiodic lattices with *unprecedented* highest global symmetry, i.e. icosahedral**
40 **symmetry.**

41 **Main**

42 Quasicrystals (QCs) are solids that possess long-range positional order with
43 crystallographically forbidden symmetries such as 5-fold, 10-fold, and 12-fold rotational
44 symmetries (Fig. 1). Since the discovery of $\text{Al}_{86}\text{Mn}_{14}$ icosahedral quasicrystal (*i* QC) in
45 1984¹, researchers have evinced tremendous interest in the physical properties of this new
46 class of ordered solids. However, no physical property directly reflecting the long-range
47 quasiperiodic order has been reported to date; in particular, no long-range magnetic order
48 has been observed thus far. Meanwhile, all magnetic-moment-bearing QCs exhibit a spin-
49 glass-like freezing behaviour without exception⁶⁻²¹. In the search for long-range magnetic
50 order in *i* QCs, researchers have particularly focused on rare-earth (*R*)-containing *i* QCs
51 with well-localised magnetic moments, such as Zn-Mg-R^{9-16} , Cd-Mg-R^{17-19} , and Cd-R
52 *i* QCs^{20,21}. However, their magnetic susceptibilities commonly display spin-freezing
53 phenomena characterised by bifurcation in the zero-field-cooled (ZFC) and field-cooled
54 (FC) susceptibilities without any accompanying sharp anomaly in the specific heat. Here,
55 it is noteworthy that both antiferromagnetism and other long-range magnetic orders such
56 as ferro- and ferrimagnetism have not been observed in real QCs.

57

58 This situation is similar to that of approximant crystals (ACs), whose atomic

59 configurations closely approximate the local atomic structures in QCs, until a decade ago
60 when antiferromagnetic transitions were discovered in Cd_6Tb 1/1 AC²² and a family of
61 Cd_6R 1/1 ACs²³. The observations of antiferromagnetic transitions and the subsequent
62 finding of ferromagnetic transitions in Au-Si-R ($R = \text{Gd, Tb, Dy, Ho}$) 1/1 ACs^{24,25} have
63 motivated us to search for magnetically ordered i QCs that are likely to exist in the vicinity
64 of the magnetic ACs. Here, to the best of our knowledge, we report on the *first* long-range
65 magnetic order in QCs, obtained by finely tuning the average electron-per-atom ratio (e/a
66 = 1.70) near which the strongest ferromagnetism (highest T_C) was recently observed for
67 Au-Al-Gd 1/1 AC²⁶.

68

69 **Search for first ferromagnetic quasicrystals**

70 In this study, Au-Ga-R alloys with various compositions in the vicinity of 1/1
71 Au-Ga-R ACs with $e/a \sim 1.70$ were rapidly quenched to search for new ferromagnetic i
72 QCs. Figure 2 presents the powder X-ray diffraction (XRD) patterns of the $\text{Au}_{65}\text{Ga}_{20}\text{R}_{15}$
73 ($R = \text{Gd, Tb}$) samples with $e/a = 1.70$; most of the peaks can be identified as i QC peaks
74 for both compounds. For both systems, some peaks are assigned to those of the 1/1 Au-
75 Ga-R AC (solid triangles). The inset displays the selected-area electron diffraction
76 patterns of i $\text{Au}_{65}\text{Ga}_{20}\text{Gd}_{15}$ with incidence along the 2-fold, 3-fold, and 5-fold rotational-

77 symmetry axes; the images clearly exhibit icosahedral symmetry features unique to *i* QCs.
78 We note here that the τ -scaling property observed in the 2-fold pattern indicates that the
79 obtained *i* QC is a primitive *i* QC, identical to the prototype *i* Cd_{5.7}Yb. Thus, we
80 successfully obtained new *i* QCs with $e/a = 1.70$, which can be regarded as candidates of
81 strong ferromagnetic *i* QCs based on the magnetic phase diagram recently obtained for
82 Au–Al–Gd 1/1 ACs²⁶ (see Fig. 5).

83

84 **Observation of ferromagnetic transitions in real quasicrystals**

85 Figures 3a and 3b show the magnetic susceptibility $\chi = M/H$ as a function of
86 the temperature below 60 K for Au₆₅Ga₂₀R₁₅ ($R = \text{Gd, Tb}$) *i* QCs, respectively, together
87 with specific heat C_p in the temperature range of 2–50 K (insets). The magnetic
88 susceptibility clearly obeys the Curie–Weiss law $\chi = N_A \mu_{\text{eff}}^2 / 3k_B (T - \theta)$ for both *i*
89 QCs, where N_A denotes the Avogadro number, k_B the Boltzmann constant, and θ the
90 Weiss temperature (see Supplementary Information). The effective magnetic moments
91 μ_{eff} obtained from the fitting are $7.90\mu_B$ for *i* Au₆₅Ga₂₀Gd₁₅ and $9.64\mu_B$ for *i*
92 Au₆₅Ga₂₀Tb₁₅, which are in good agreement with the theoretical values of R^{3+} ($R = \text{Gd,}$
93 Tb) free ions, $7.94\mu_B$ and $9.72\mu_B$, respectively. Thus, the magnetic moments are strongly
94 localised on the R^{3+} ions, as in the cases of the other *R*-containing *i* QCs. A distinct

95 difference from the previously reported R -containing i QCs lies in the sign of θ as a
96 consequence of fine-tuning the e/a ratio to 1.70, for which we obtained a strongly
97 ferromagnetic 1/1 AC; the θ values are 27.9 K for i Au₆₅Ga₂₀Gd₁₅ and 12.9 K for i
98 Au₆₅Ga₂₀Tb₁₅, which clearly demonstrate that the inter-spin interactions are expectedly
99 strongly *ferromagnetic* for these i QCs; this result is in contrast with the negative θ
100 values exclusively observed for all the other i QCs reported to date (see Fig.5).

101

102 From Figs. 3a and 3b, we note that χ increases sharply at 23.4 K and 16.0 K for
103 the Au₆₅Ga₂₀ R ₁₅ ($R = \text{Gd, Tb}$) i QCs, respectively, suggesting the occurrence of a
104 ferromagnetic transition for both i QCs. For i Au₆₅Ga₂₀Tb₁₅, a deviation of χ between
105 the FC and ZFC susceptibilities is observed below 16.0 K; this behaviour is similar to
106 that observed for Tb-containing ACs^{25,27}. The M - H curves for Au₆₅Ga₂₀ R ₁₅ ($R = \text{Gd, Tb}$)
107 i QCs under fields up to 7 T at 2 K are provided in the Supplementary Information. For i
108 Au₆₅Ga₂₀Gd₁₅, M quickly saturates to $\sim 7\mu_{\text{B}}/\text{Gd}^{3+}$, nearly the full moment of a free Gd³⁺
109 ion ($7\mu_{\text{B}}/\text{Gd}^{3+}$), at a low field of 100 Oe. On the other hand, for i Au₆₅Ga₂₀Tb₁₅, the M
110 magnitude is suppressed to $\sim 6\mu_{\text{B}}/\text{Tb}^{3+}$ at 7 T, about two-thirds of the full moment of a
111 Tb³⁺ ion ($9\mu_{\text{B}}/\text{Tb}^{3+}$). This behaviour is closely consistent with those of Tb-containing
112 ACs²⁵⁻²⁷, which was attributed to the existence of the strong uniaxial anisotropy of the

113 Tb^{3+} spins. The M suppression is ascribed to the formation of non-coplanar spin
114 configuration due to this strong uniaxial anisotropy of Tb^{3+} spins in Au–Si–Tb 1/1 AC²⁸.
115 The insets of Figs. 3a and 3b show the variation in specific heat C_p of the $\text{Au}_{65}\text{Ga}_{20}\text{R}_{15}$ (R
116 = Gd, Tb) i QCs, respectively. For i $\text{Au}_{65}\text{Ga}_{20}\text{Gd}_{15}$, C_p clearly displays a λ -shaped
117 anomaly at 23.1 K, which corresponds to the sharp increase in χ at 23.4 K; this result
118 validates the magnetic-transition occurrence at $T_C = 23$ K. In contrast, for i $\text{Au}_{65}\text{Ga}_{20}\text{Tb}_{15}$,
119 C_p exhibits a broad anomaly around 16 K, close to the temperature corresponding to the
120 sharp rise in χ .

121

122 **Verification of the ferromagnetism in i $\text{Au}_{65}\text{Ga}_{20}\text{Tb}_{15}$ by neutron-diffraction** 123 **experiments**

124 To unambiguously prove the occurrence of long-range magnetic order in i
125 $\text{Au}_{65}\text{Ga}_{20}\text{Tb}_{15}$, we next performed neutron-diffraction experiments. Figure 4a shows
126 powder-neutron-diffraction patterns of i $\text{Au}_{65}\text{Ga}_{20}\text{Tb}_{15}$ measured at $T = 3.5$ K and 20 K,
127 which are below and above the anomaly temperature of 16 K observed in the χ – T and
128 C_p – T curves. Diffraction patterns measured at various temperatures are provided in the
129 Supplementary Information. We clearly observe magnetic Bragg reflections at the base
130 temperature of 3.5 K. Some magnetic reflections newly appear at the base temperature,

131 while many others are observed as an enhancement of the nuclear reflections (211111,
132 221001, and 332002, to note a few), confirming the ferromagnetic nature of the magnetic
133 order. We note that several magnetic peaks at low angles are due to the contaminating 1/1
134 Au-Ga-Tb AC, inclusion of which is detected in the XRD pattern (as denoted by the
135 triangles in Fig. 2). Details of the appearance of the magnetic Bragg peaks from the 1/1
136 AC phase are given in the Supplementary Information, where the powder-neutron-
137 diffraction pattern of the Au-Ga-Tb 1/1 AC of the same nominal composition prepared
138 by additional annealing at 923 K for 50 h is provided. Here, it is noted that the magnetic
139 reflections from the 1/1 Au-Ga-Tb AC can be consistently indexed with the cubic
140 commensurate indices (see Fig. S4). In addition, due to the loss of the bcc symmetry by
141 the magnetic order, similar to the whirling magnetic order discovered in the 1/1 Au-Al-
142 Tb AC²⁹, the magnetic reflections from the 1/1 Au-Ga-Tb AC appear separately from its
143 nuclear reflections. In the *i* Au₆₅Ga₂₀Tb₁₅ QC shown in Fig. 4a, we clearly observe
144 reflections that cannot be assigned to those of the 1/1 AC and that are located exactly at
145 the positions of the nuclear Bragg reflections of the *i* QC, such as the 111000 and 111100
146 reflections (as newly appearing magnetic reflections), and 211111, 221001 and 332002
147 reflections (as reflections appearing on the nuclear-reflection positions). Figure 4b
148 magnifies the low- 2θ region between 30° – 33°, wherein we observe the development of

149 the strongest 111000 magnetic Bragg reflection with decreasing temperature below $T_C =$
150 16 K, which indicates ferromagnetic order formation in $i\text{Au}_{65}\text{Ga}_{20}\text{Tb}_{15}$. Figure 4c shows
151 the temperature evolution of the 111000 magnetic Bragg reflection intensity, wherein T_C
152 is estimated using the critical exponent fit as $T_C = 16.1(3)$ K, which is in excellent
153 agreement with the Curie temperature of $T_C = 16$ K observed in the bulk magnetic
154 measurements. Here, we note that *this is the first direct microscopic observation of long-*
155 *range magnetic order in a QC via neutron-diffraction experiments.* The next epoch-
156 making issue is to determine the complex magnetic structure of Au–Ga–Tb i QC. This
157 requires the development of analysis methods and algorithms for the magnetic-structure
158 determination of ferromagnetic i QCs via higher-dimensional crystallography.

159

160 **Discussion and conclusion**

161 Next, we discuss the reason for the formation of the ferromagnetic QCs in the
162 present $\text{Au}_{65}\text{Ga}_{20}\text{R}_{15}$ ($R = \text{Gd}, \text{Tb}$) compounds. According to the theory underlying the
163 Ruderman–Kittel–Kasuya–Yosida (RKKY) interaction³⁰, which is the major magnetic
164 interaction between R^{3+} spins for R -containing QCs, the RKKY interaction magnitude
165 scales with the de-Gennes factor (dG) $[(g_J - 1)^2 J(J + 1)]$, where g_J denotes the Landé
166 g-factor and J the total angular momentum. Figure 5 shows the normalised Weiss

167 temperature, θ/dG , as a function of the e/a ratio over a wide e/a range from 1.5 to 2.2
168 for all the R -containing Tsai-type i QCs reported to date^{17,20,31}, together with the θ/dG
169 values for the Au–Al–Gd 1/1 ACs (orange circles) for comparison²⁶. The figure also
170 shows the magnetic-ground-state regime of the Au–Al–Gd 1/1 AC in terms of the e/a
171 ratio, wherein we note that the magnetic order changes from antiferromagnetic to
172 ferromagnetic and then to spin glass (SG) with increasing e/a ratio. From Fig. 5, we
173 clearly observe that the magnitude of the θ/dG value and its sign are sensitively and
174 systematically dependent on the e/a ratio for the AC. Consequently, it is clear that the
175 negative θ values exclusively observed for previously reported i QCs are attributed to
176 their relatively large e/a values of 2.10 - 2.15, around which spin-glass-like behaviours
177 are predominantly observed for both QCs and ACs. In contrast, the large positive θ
178 values for the present Au–Ga– R i QCs suggest that their e/a ratios (=1.70) correspond to
179 the middle of the ferromagnetic regime of the Au–Al–Gd 1/1 AC. Thus, our successful
180 synthesis of ferromagnetic QCs justifies that the magnetic phase diagram obtained for
181 ACs also holds for i QCs. This result means that *we have also obtained the long-sought*
182 *conditions for realising various magnetic orders including antiferromagnetic i QCs.*
183 Moreover, our findings have shown that the Weiss temperature (or net magnetic
184 interaction) is also tuneable for i QCs via the tuning of the e/a ratio. Consequently, the

185 quest for the first antiferromagnetic *i* QCs can now progress along this research line.

186

187 Ferromagnetic $\text{Au}_{65}\text{Ga}_{20}\text{R}_{15}$ ($R = \text{Gd}, \text{Tb}$) *i* QCs are ordered solids with the
188 highest possible symmetry, i.e. icosahedral symmetry; these QCs have not been
189 synthesised previously. Hence, Au–Ga–*R i* QCs are the most isotropically ordered
190 magnets among all materials discovered to date. For the icosahedral point groups (*I* and
191 *I_h*), there exist six 5-fold, ten 3-fold, and fifteen 2-fold axes, and accordingly, there can
192 be 6, 10, and 15 easy axes, respectively, depending on the easy magnetisation direction.
193 The existence of such a large number of equivalent easy axes can result in significantly
194 low energy barriers between the neighbouring easy axes (as observed in cubic soft
195 magnets), which can lead to the more pronounced easy rotation of magnetic moments.
196 From the technological viewpoint, isotropic materials should exhibit zero
197 magnetocrystalline anisotropy energy, which results in low coercivity, low hysteresis loss,
198 and high permeability. For icosahedral symmetry, the magnetic anisotropy energy is only
199 associated with the higher-order terms (sixth-order and higher). In contrast, conventional
200 crystals of the highest symmetry, i.e. cubic symmetry, where the fourth-order terms are
201 nonzero, exhibit crystal anisotropy as the lower-order terms mostly contribute to the
202 magnetic anisotropy. Thus, it would be a challenging issue to eliminate the sixth-order

203 terms in the ferromagnetic i QC by tuning structural parameters via tweaking the e/a ratio
204 and/or by isovalent substitution.

205

206 Finally, our successful synthesis of ferromagnetic i QCs shows that e/a tuning is
207 effective in controlling the QC magnetism and that various exotic magnetic orders
208 reflecting quasiperiodicity and/or high global/local symmetry can now be achieved by
209 simply varying the e/a ratio. Moreover, our study opens pathways for the fundamental
210 and technological exploration of the intrinsic nature of magnetic i QCs across various
211 disciplines.

212 **References**

- 213 1. Shechtman, D., Blech, D., Gratias, D. & Chan, J. W. Metallic phase with long-range
214 orientational order and no translational symmetry. *Phys. Rev. Lett.* **53**, 1951–1953
215 (1984).
- 216 2. Takakura, H., Gómez, C. P., Yamamoto, A., de Boissieu, M. & Tsai, A. P. Atomic
217 structure of the binary icosahedral Yb-Cd quasicrystal. *Nat. Mat.* **6**, 58–63 (2007).
- 218 3. Yamada, T. *et al.* Synthesis and Atomic Structure of the Yb–Ga–Au 1/1 Quasicrystal
219 Approximant. *Inorg. Chem.* **58**, 6320-6327 (2019).
- 220 4. Gómez, C. P., & Lidin, S. Structure of Ca₁₃Cd₇₆: A novel approximant to the MCd_{5.7}
221 quasicrystals (M= Ca, Yb). *Angew. Chem. Int. Ed* **40**, 4037-4039 (2011).
- 222 5. Momma, K., & Izumi, F. VESTA 3 for three-dimensional visualization of crystal,
223 volumetric and morphology data. *J. Appl. Crystallogr.* **44**, 1272-1276 (2011).
- 224 6. Fukamichi, K. *et al.* Magnetic and electrical properties of icosahedral quasicrystalline
225 Al-Mn alloys. *J. Phys. F: Met. Phys.* **16**, 1059 (1986).
- 226 7. Hauser, J. J., Chen, H. S., & Waszczak, J. V. Magnetic properties of Al-Si-Mn and Al-
227 Mn quasicrystals and amorphous films. *Phys. Rev. B* **33**, 3577 (1986).
- 228 8. Hippert, F., & Prejean, J. J. Magnetism in quasicrystals. *Philos. Mag.* **88**, 2175-2190
229 (2008).

- 230 9. Hattori, Y. *et al.* Spin-glass behaviour of icosahedral Mg-Gd-Zn and Mg-Tb-Zn
231 quasi-crystals. *J. Phys.: Condens. Matter.* **7**, 2313 (1995).
- 232 10. Hattori, Y. *et al.* Electronic specific heat coefficient and magnetic entropy of
233 icosahedral Mg-RE-Zn (RE= Gd, Tb and Y) quasicrystals. *J. Phys.: Condens. Matter.* **7**,
234 4183 (1995).
- 235 11. Charrier, B., & Schmitt, D. Magnetic properties of R₈Mg₄₂Zn₅₀ quasicrystals (R=
236 Tb, Dy, Ho, Er). *J. Magn. Magn. Mater.* **171**, 106-112 (1997).
- 237 12. Islam, Z. *et al.* Reinvestigation of long-range magnetic ordering in icosahedral Tb-
238 Mg-Zn. *Phys. Rev. B* **57**, R11047 (1998).
- 239 13. Sato, T. J., Takakura, H., Tsai, A. P., & Shibata, K. Anisotropic spin correlations in
240 the Zn-Mg-Ho icosahedral quasicrystal. *Phys. Rev. Lett.* **81**, 2364 (1998).
- 241 14. Fisher, I. R. *et al.* Magnetic and transport properties of single-grain R-Mg-Zn
242 icosahedral quasicrystals [R= Y, (Y_{1-x} Gd_x), (Y_{1-x} Tb_x), Tb, Dy, Ho, and Er]. *Phys. Rev.*
243 *B* **59**, 308 (1999).
- 244 15. Sato, T. J. *et al.* Antiferromagnetic spin correlations in the Zn-Mg-Ho icosahedral
245 quasicrystal. *Phys. Rev. B* **61**, 476 (2000).

- 246 16. Dolinšek, J., Jagličić, Z., Chernikov, M. A., Fisher, I. R., & Canfield, P. C. Unusual
247 spin-glass phase in icosahedral Tb-Mg-Zn quasicrystals. *Phys. Rev. B* **64**, 224209
248 (2001).
- 249 17. Sato, T. J., Guo, J., & Tsai, A. P. Magnetic properties of the icosahedral Cd-Mg-rare-
250 earth quasicrystals. *J. Phys.: Condens. Mater.* **13**, L105 (2001).
- 251 18. Sato, T. J., Takakura, H., Guo, J., Tsai, A. P., & Ohoyama, K. Magnetic correlations
252 in the Cd–Mg–Tb icosahedral quasicrystal. *J. Alloys Compd.* **342**, 365-368 (2002).
- 253 19. Sebastian, S. E., Huie, T., Fisher, I. R., Dennis, K. W., & Kramer, M. J. Magnetic
254 properties of single grain R–Mg–Cd primitive icosahedral quasicrystals (R= Y, Gd, Tb
255 or Dy). *Philos. Mag.* **84**, 1029-1037 (2004).
- 256 20. Goldman, A. I. *et al.* A family of binary magnetic icosahedral quasicrystals based on
257 rare earths and cadmium. *Nat. Mater.* **12**, 714-718 (2013).
- 258 21. Kong, T. *et al.* Magnetic and transport properties of i-R-Cd icosahedral quasicrystals
259 (R= Y, Gd-Tm). *Phys. Rev. B* **90**, 014424 (2014).
- 260 22. Tamura, R., Muro, Y., Hiroto, T., Nishimoto, K., & Takabatake, T. Long-range
261 magnetic order in the quasicrystalline approximant Cd₆Tb. *Phys. Rev. B* **82**, 220201
262 (2010).

- 263 23. Mori, A. *et al.* Electrical and magnetic properties of quasicrystal approximants RCd_6
264 (R: rare earth). *J. Phys. Soc. Jpn.* **81**, 024720 (2012).
- 265 24. Hiroto, T. *et al.* Ferromagnetism and re-entrant spin-glass transition in quasicrystal
266 approximants Au–SM–Gd (SM= Si, Ge). *J. Phys.: Condens. Matter.* **25**, 426004 (2013).
- 267 25. Hiroto, T., Tokiwa, K., & Tamura, R. Sign of canted ferromagnetism in the
268 quasicrystal approximants Au-SM-R (SM= Si, Ge and Sn/R= Tb, Dy and Ho). *J. Phys.:*
269 *Condens. Matter.* **26**, 216004 (2014).
- 270 26. Ishikawa, A. *et al.* Antiferromagnetic order is possible in ternary quasicrystal
271 approximants. *Phys. Rev. B* **98**, 220403 (2018).
- 272 27. Gebresenbut, G. H., Andersson, M. S., Nordblad, P., Sahlberg, M., & Pay Gómez, C.
273 Tailoring magnetic behavior in the Tb-Au-Si quasicrystal approximant system. *Inorg.*
274 *Chem.* **55**, 2001-2008 (2016).
- 275 28. Hiroto, T. *et al.* Noncoplanar ferrimagnetism and local crystalline-electric-field
276 anisotropy in the quasicrystal approximant $\text{Au}_{70}\text{Si}_{17}\text{Tb}_{13}$. *J. Phys.: Condens. Matter.* **32**
277 415802 (2020).
- 278 29. Sato, T. J. *et al.* Whirling spin order in the quasicrystal approximant $\text{Au}_{72}\text{Al}_{14}\text{Tb}_{14}$.
279 *Phys. Rev. B* **100**, 054417 (2019).
- 280 30. Yosida, K. Magnetic properties of Cu-Mn alloys. *Phys. Rev.* **106**, 893 (1957).

- 281 31. Stadnik, Z. M., Al-Qadi, K., & Wang, P. Magnetic properties and ^{155}Gd Mössbauer
282 spectroscopy of the icosahedral quasicrystal $\text{Ag}_{50}\text{In}_{36}\text{Gd}_{14}$. *J. Phys.: Condens. Matter*.
283 **19**, 326208 (2007).
- 284 32. Avdeev, M., & Hester, J. R. ECHIDNA: a decade of high-resolution neutron powder
285 diffraction at OPAL. *J. Appl. Crystallogr.* **51**, 1597-1604 (2018).

286 **Figure legends**

287 **Figure 1 | Atomic structure of the Tsai-type icosahedral quasicrystal.**

288 **a**, Arrangement of the rare-earth (*R*) atoms viewed along a 5-fold axis. The *R* atoms in
289 blue (84.57% of the total *R* atoms) are located at the vertices of the icosahedra whereas
290 those in silver (15.43%) are situated inside the acute rhombohedra (shown at the bottom
291 of **b**). **b**, Five successive concentric clusters that form the rhombic triacontahedral
292 (RTH) cluster (top) and acute rhombohedron (bottom). The atoms in blue and silver
293 represent the same *R* atoms shown in **a** whereas those in gold and red denote Au and Ga
294 atoms, respectively. The cluster structure is illustrated based on the structure model of
295 the Cd–Yb QC² and Au–Ga–Yb 1/1 approximant³, and the acute rhombohedron is
296 drawn based on the structure model of the Cd–Ca 2/1 approximant⁴. This image was
297 obtained by using the VESTA 3 program package⁵.

298

299 **Figure 2 | Powder X-ray diffraction patterns for Au₆₅Ga₂₀Gd₁₅ and Au₆₅Ga₂₀Tb₁₅**

300 **samples.** Mother alloys of various compositions near $e/a = 1.70$, prepared by arc-
301 melting, were subjected to rapid quenching onto a Cu wheel rotating at 4000 rpm. As
302 shown in the patterns, icosahedral quasicrystals (*i* QCs) are formed for Au₆₅Ga₂₀*R*₁₅ (*R*
303 = Gd, Tb) compositions with $e/a = 1.70$. Most of the peaks are indexed as those of a

304 primitive i QC, indicating that a nearly single-phase i QC is formed for both samples.
305 The peaks denoted by the triangles are from the $1/1$ Au–Ga– R approximant. The inset
306 displays selected-area electron diffraction patterns of $\text{Au}_{65}\text{Ga}_{20}\text{Gd}_{15}$ along the (a) 2-fold,
307 (b) 3-fold, and (c) 5-fold axes, depicting the formation of an i QC.

308

309 **Figure 3 | Temperature dependences of the FC and ZFC magnetic susceptibilities, χ**
310 **= M/H , for (a) the $\text{Au}_{65}\text{Ga}_{20}\text{Gd}_{15}$ and (b) $\text{Au}_{65}\text{Ga}_{20}\text{Tb}_{15}$ i QCs.** FC and ZFC magnetic
311 susceptibilities measured under 10 Oe are shown in the temperature range of 2–60 K. The
312 insets show temperature dependences of specific heat, C_p , for $\text{Au}_{65}\text{Ga}_{20}R_{15}$ ($R = \text{Gd}, \text{Tb}$)
313 i QCs, respectively. For the $\text{Au}_{65}\text{Ga}_{20}\text{Gd}_{15}$ i QC, a λ -shaped anomaly is observed at 23.1
314 K, clearly indicating a magnetic-transition occurrence, whereas a broad anomaly is
315 observed around 16 K for the $\text{Au}_{65}\text{Ga}_{20}\text{Tb}_{15}$ i QC, suggesting the occurrence of a magnetic
316 transition. In the inset of **b**, the Curie temperature T_C is estimated from the peak position
317 of the dC_p/dT curve.

318

319 **Figure 4 | (a,b,c) Powder-neutron-diffraction patterns of the $\text{Au}_{65}\text{Ga}_{20}\text{Tb}_{15}$ i QC.**

320 In **a**, neutron-diffraction patterns measured at the base temperature (3.5 K) and the
321 paramagnetic temperature (20 K), which are below and above $T_C = 16$ K inferred from

322 the bulk measurements, are shown, together with the nuclear peak positions and their
323 6D indices for the *i* QC calculated with the 6D lattice constant $a_{6D} = 5.2966 \text{ \AA}$. The low-
324 2θ region, which contains the strongest magnetic peak from the *i* QC, is magnified in **b**.
325 Magnetic 111000 peak is clearly observed at $2\theta = 31.8$ below T_C and disappears above
326 T_C , evidencing the formation of long-range magnetic order in the $\text{Au}_{65}\text{Ga}_{20}\text{Tb}_{15}$ *i* QC.
327 The temperature dependence of the integrated intensity of the 111000 reflection is
328 plotted in **c**, in which the critical exponent fit [$I \propto (1 - T/T_C)^{2\beta}$] gives an estimate of the
329 transition temperature as $T_C = 16.1(3) \text{ K}$.

330

331 **Figure 5 | Normalised Weiss temperature, θ/dG , and the magnetic ground state as**
332 **a function of the e/a ratio.** The θ/dG values are plotted over a wide e/a range between
333 1.5 and 2.2 for all the *R*-containing Tsai-type *i* QCs reported to date, together with the
334 θ/dG values reported for the Au–Al–Gd 1/1 AC (orange circles) for comparison. The
335 magnetic ground state of the Au–Al–Gd 1/1 AC is also shown. The θ/dG values of the
336 present Au–Ga–*R* (*R* = Gd, Tb) *i* QCs are large positive values, whereas those for the
337 previously reported *i* QCs are large negative values without exception. This dependence
338 of the θ/dG value on the e/a ratio is in good agreement with the behaviour observed in
339 the Au–Al–Gd 1/1 AC.

340 **Methods**

341 **Sample preparation and macroscopic measurements.** Ternary (Au,Ga)₈₅R₁₅ (*R* = Gd,
342 Tb) alloys with various Au/Ga ratios were prepared by arc-melting high-purity Au
343 (99.99 wt%), Ga (99.9999 wt%), Gd (99.9 wt%), and Tb (99.9 wt%) raw elements.
344 Nominal compositions were selected to ensure that electron-per-atom ratio (*e/a*) was
345 close to 1.70, which corresponds to the near-centre of the ferromagnetic regime recently
346 obtained for Au–Al–Gd 1/1 ACs¹³. The alloys were then rapidly quenched onto a Cu
347 wheel rotating at 4000 rpm. The phase purity of the samples was examined via powder
348 X-ray diffraction (Rigaku MiniFlex 600) with Cu *K*α radiation. Electron diffraction
349 patterns were acquired by using a JEM-2010HC (JEOL Ltd.) microscope. The magnetic
350 properties were measured by using a magnetic property measurement system (MPMS;
351 Quantum Design) in the temperature range of 2–300 K under magnetic fields up to 7 T.
352 Specific-heat measurements were performed by using a physical property measurement
353 system (PPMS; Quantum Design) via the relaxation method between 2 and 50 K.

354

355 **Neutron-diffraction experiments.** Neutron-powder-diffraction experiments were
356 performed by using the high-resolution powder diffractometer ECHIDNA installed at
357 the OPAL reactor²⁸, Australian Nuclear Science and Technology Organization. Neutrons

358 with $\lambda = 2.4395 \text{ \AA}$ were selected by using the Ge 331 reflections. The powder sample
359 was loaded in a $\phi 6$ mm vanadium can and then set in a closed-cycle ^4He refrigerator
360 with the base temperature of 3.5 K.

361

362 **Acknowledgements**

363 We acknowledge and thank S. Yoshida for assistance with the neutron-diffraction
364 experiments. This work was supported by JSPS KAKENHI Grant Numbers
365 JP19H05817 and JP19H05818.

366

367 **Author contributions**

368 R.T. and T.J.S. designed and conducted the experiments; A.I., A.K. and S.S. synthesized
369 the samples, and performed the magnetization measurements; T.Y., T.S. and N.S.
370 performed characterization of the samples; T.F. performed specific heat measurements;
371 C.W.W., M.A., T.J.S. and A.I. performed neutron-diffraction experiments; R.T. drafted
372 the manuscript and all authors participated in the writing and review of the final draft.

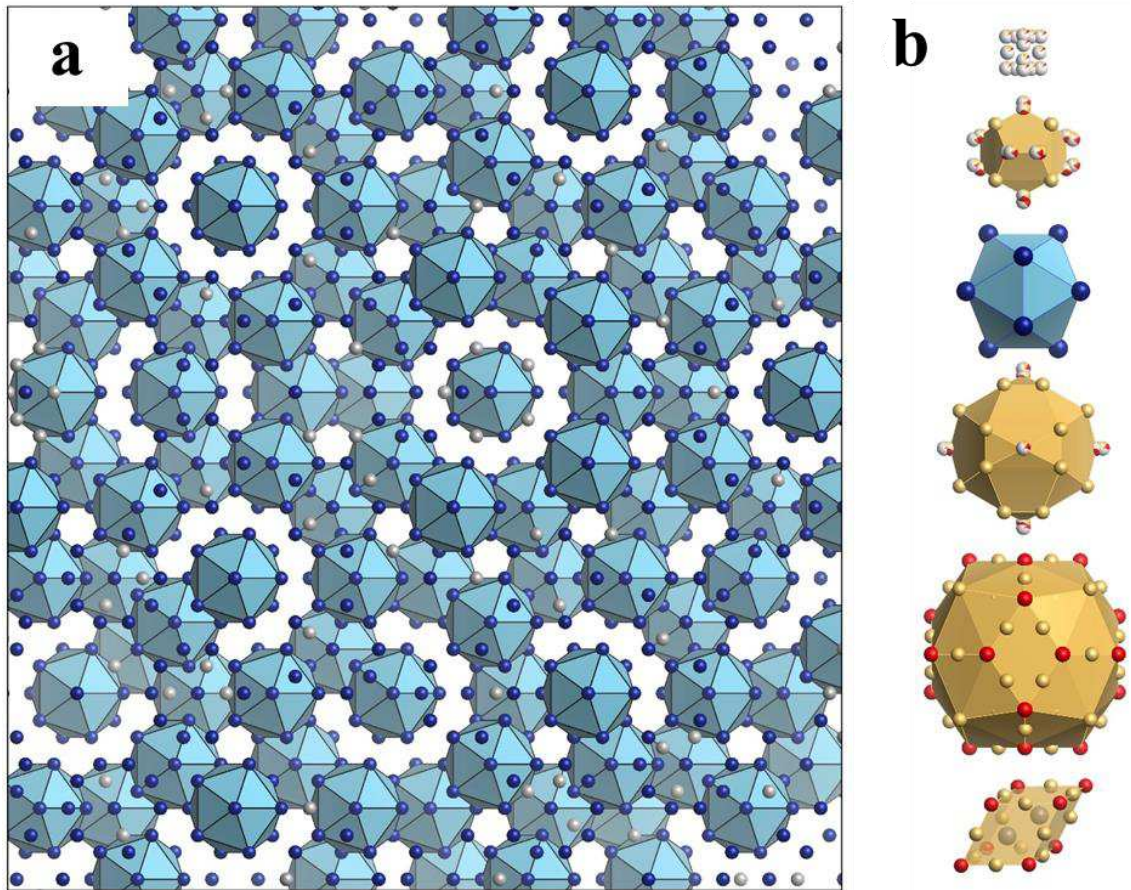
373

374 **Additional information**

375 Correspondence and requests for materials should be addressed to R.T. or T.J.S.

376 **Competing financial interests**

377 The authors declare no competing financial interests.



378

379

380 **Figure 1 | Atomic structure of the Tsai-type icosahedral quasicrystal.**

381 **a**, Arrangement of the rare-earth (*R*) atoms viewed along a 5-fold axis. The *R* atoms in

382 blue (84.57% of the total *R* atoms) are located at the vertices of the icosahedra whereas

383 those in silver (15.43%) are situated inside the acute rhombohedra (shown at the bottom

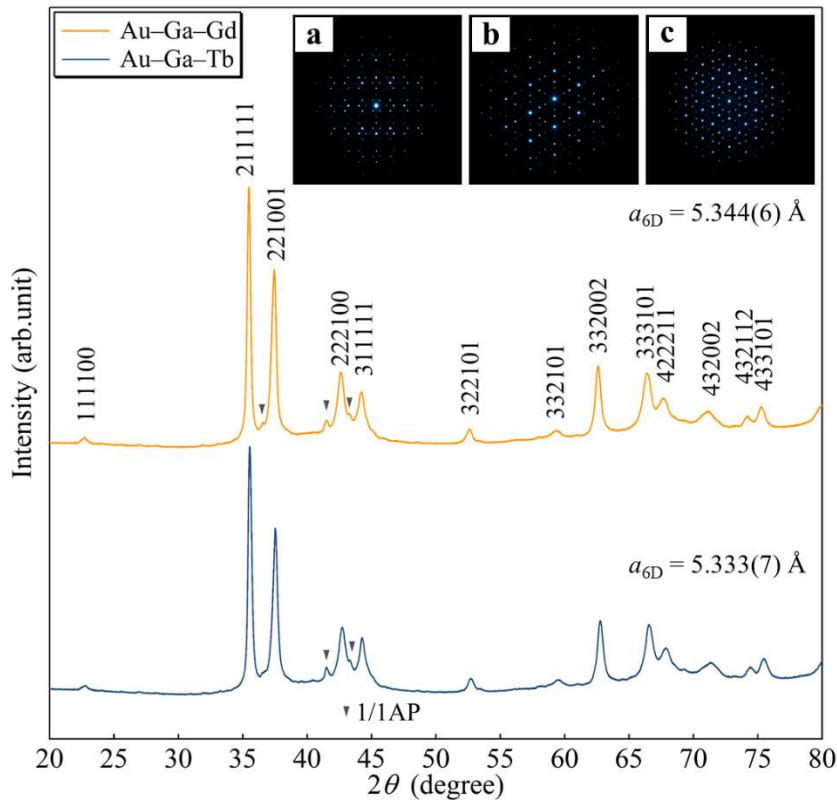
384 of **b**). **b**, Five successive concentric clusters that form the rhombic triacontahedral

385 (RTH) cluster (top) and acute rhombohedron (bottom). The atoms in blue and silver

386 represent the same *R* atoms shown in **a** whereas those in gold and red denote Au and Ga

387 atoms, respectively. The cluster structure is illustrated based on the structure model of
388 the Cd–Yb QC² and Au–Ga–Yb 1/1 approximant³, and the acute rhombohedron is
389 drawn based on the structure model of the Cd–Ca 2/1 approximant⁴. This image was
390 obtained by using the VESTA 3 program package⁵.

391



392

393

394 **Figure 2 | Powder X-ray diffraction patterns for $\text{Au}_{65}\text{Ga}_{20}\text{Gd}_{15}$ and $\text{Au}_{65}\text{Ga}_{20}\text{Tb}_{15}$**

395 **samples.** Mother alloys of various compositions near $e/a = 1.70$, prepared by arc-

396 melting, were subjected to rapid quenching onto a Cu wheel rotating at 4000 rpm. As

397 shown in the patterns, icosahedral quasicrystals (*i* QCs) are formed for $\text{Au}_{65}\text{Ga}_{20}R_{15}$ (R

398 = Gd, Tb) compositions with $e/a = 1.70$. Most of the peaks are indexed as those of a

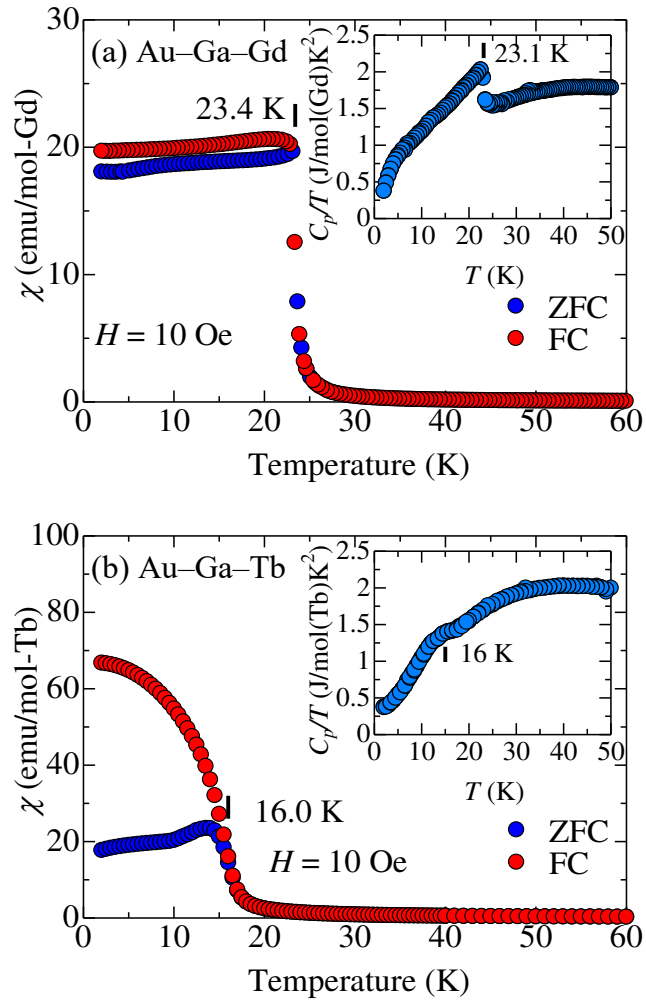
399 primitive *i* QC, indicating that a nearly single-phase *i* QC is formed for both samples.

400 The peaks denoted by the triangles are from the 1/1 Au–Ga– R approximant. The inset

401 displays selected-area electron diffraction patterns of $\text{Au}_{65}\text{Ga}_{20}\text{Gd}_{15}$ along the (a) 2-fold,

402 (b) 3-fold, and (c) 5-fold axes, depicting the formation of an *i* QC.

403



404

405

406 **Figure 3 | Temperature dependences of the FC and ZFC magnetic susceptibilities, χ**

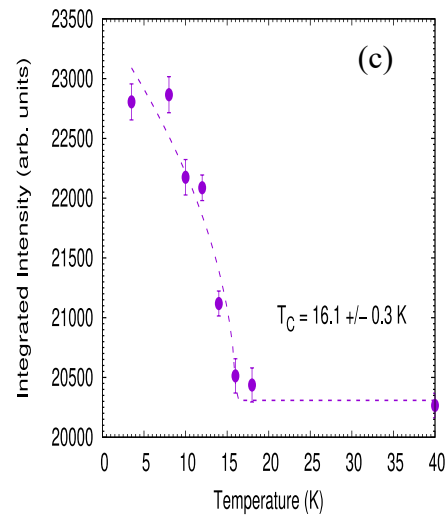
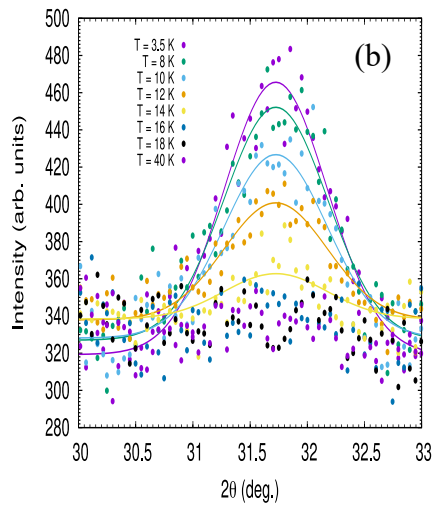
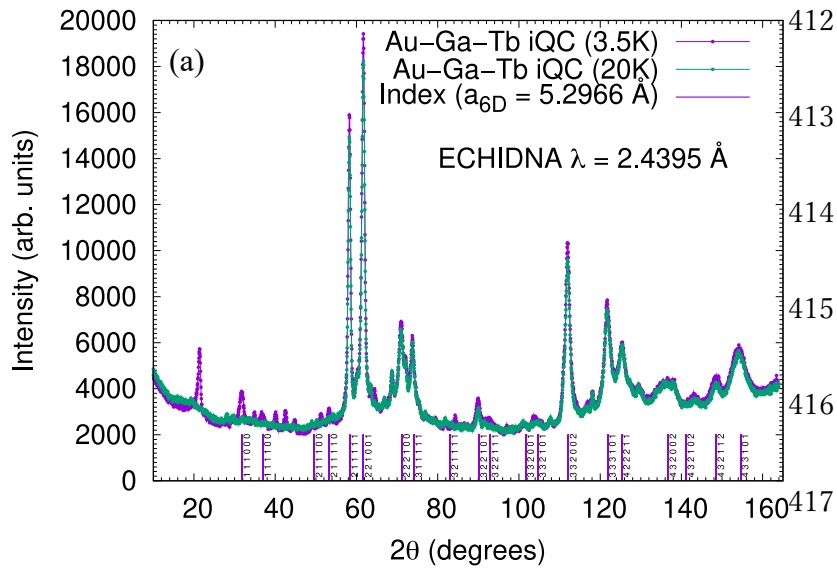
407 **= M/H , for (a) the Au₆₅Ga₂₀Gd₁₅ and (b) Au₆₅Ga₂₀Tb₁₅ *i* QCs. FC and ZFC magnetic**

408 **susceptibilities measured under 10 Oe are shown in the temperature range of 2–60 K. The**

409 **insets show temperature dependences of specific heat, C_p . In both insets, the Curie**

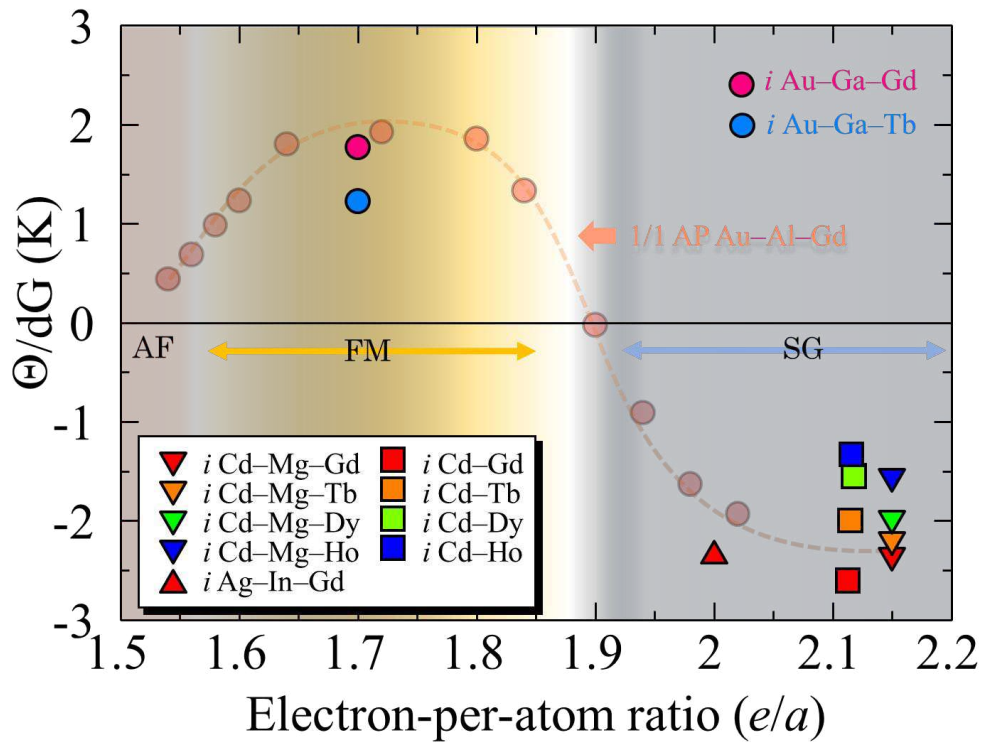
410 **temperature T_C was estimated from the peak position of the dC_p/dT curve.**

411



423 **Figure 4 | (a,b,c) Powder-neutron-diffraction patterns of the $\text{Au}_{65}\text{Ga}_{20}\text{Tb}_{15}$ *i* QC.**
 424 In **a**, neutron-diffraction patterns measured at the base temperature (3.5 K) and the
 425 paramagnetic temperature (20 K), which are below and above $T_C = 16$ K inferred from
 426 the bulk measurements, are shown, together with the nuclear peak positions and their
 427 6D indices for the *i* QC calculated with the 6D lattice constant $a_{6D} = 5.2966$ Å. The low-
 428 2θ region, which contains the strongest magnetic peak from the *i* QC, is magnified in **b**.

429 Magnetic 111000 peak is clearly observed at $2\theta = 31.8$ below T_C and disappears above
430 T_C , evidencing the formation of long-range magnetic order in the $\text{Au}_{65}\text{Ga}_{20}\text{Tb}_{15}$ *i* QC.
431 The temperature dependence of the integrated intensity of the 111000 reflection is
432 plotted in **c**, in which the critical exponent fit [$I \propto (1 - T/T_C)^{2\beta}$] gives an estimate of the
433 transition temperature as $T_C = 16.1(3)$ K.
434



435

436

437 **Figure 5 | Normalised Weiss temperature, Θ/dG , and the magnetic-ground-state**
 438 **regime as a function of the e/a ratio.** The Θ/dG values are plotted over a wide e/a
 439 range between 1.5 and 2.2 for all the R -containing Tsai-type i QCs reported to date,
 440 together with the Θ/dG values reported for the Au–Al–Gd 1/1 AC (orange circles) for
 441 comparison. The magnetic-ground-state regime of the Au–Al–Gd 1/1 AC is also shown.
 442 The Θ/dG values of the present Au–Ga– R ($R = \text{Gd}, \text{Tb}$) i QCs are large positive values,
 443 whereas those for the previously reported i QCs are large negative values without
 444 exception. This dependence of the Θ/dG value on the e/a ratio is in good agreement
 445 with the behaviour observed in the Au–Al–Gd 1/1 AC.

Figures

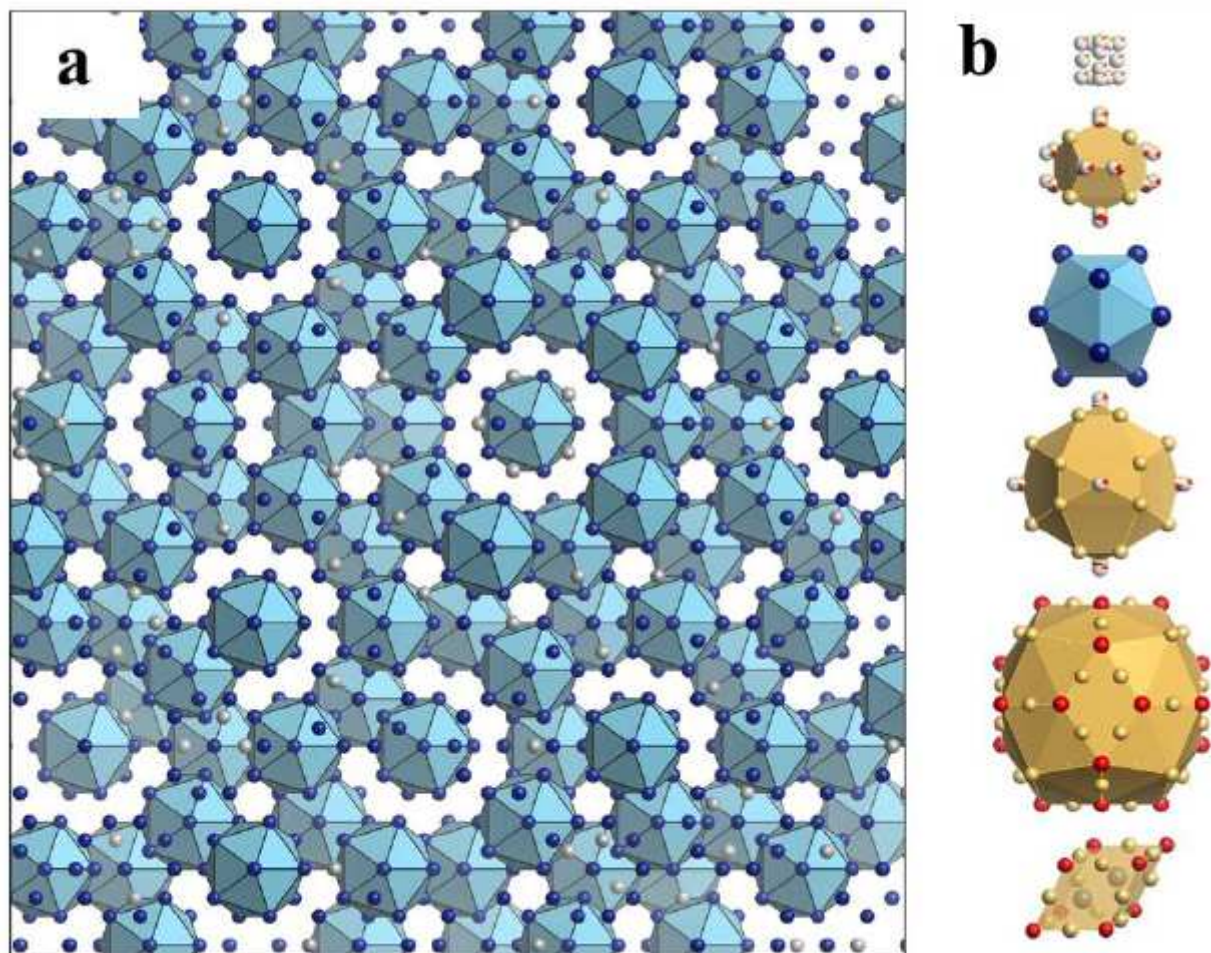


Figure 1

Atomic structure of the Tsai-type icosahedral quasicrystal. a, Arrangement of the rare-earth (R) atoms viewed along a 5-fold axis. The R atoms in blue (84.57% of the total R atoms) are located at the vertices of the icosahedra whereas those in silver (15.43%) are situated inside the acute rhombohedra (shown at the bottom of b). b, Five successive concentric clusters that form the rhombic triacontahedron (RTH) cluster (top) and acute rhombohedron (bottom). The atoms in blue and silver represent the same R atoms shown in a whereas those in gold and red denote Au and Ga atoms, respectively. The cluster structure is illustrated based on the structure model of the Cd–Yb QC₂ and Au–Ga–Yb 1/1 approximant³, and the acute rhombohedron is drawn based on the structure model of the Cd–Ca 2/1 approximant⁴. This image was obtained by using the VESTA 3 program package⁵.

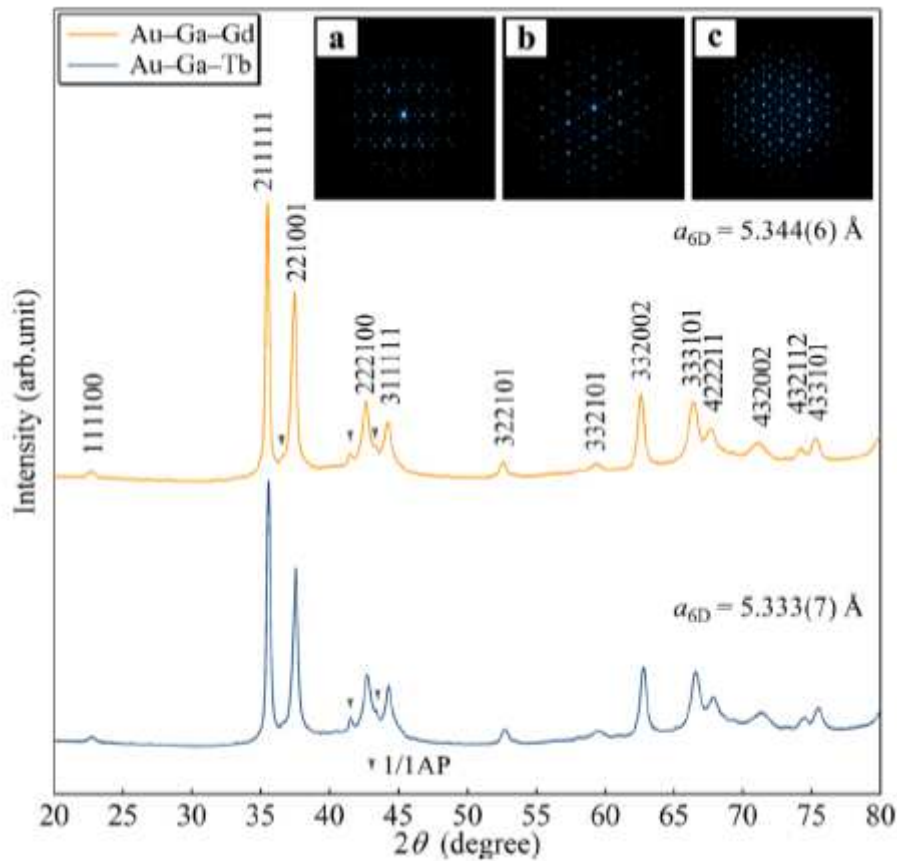


Figure 2

Powder X-ray diffraction patterns for Au₆₅Ga₂₀Gd₁₅ and Au₆₅Ga₂₀Tb₁₅ samples. Mother alloys of various compositions near $e/a = 1.70$, prepared by arc-melting, were subjected to rapid quenching onto a Cu wheel rotating at 4000 rpm. As shown in the patterns, icosahedral quasicrystals (i QCs) are formed for Au₆₅Ga₂₀R₁₅ (R = Gd, Tb) compositions with $e/a = 1.70$. Most of the peaks are indexed as those of a primitive i QC, indicating that a nearly single-phase i QC is formed for both samples. The peaks denoted by the triangles are from the 1/1 Au-Ga-R approximant. The inset displays selected-area electron diffraction patterns of Au₆₅Ga₂₀Gd₁₅ along the (a) 2-fold, (b) 3-fold, and (c) 5-fold axes, depicting the formation of an i QC.

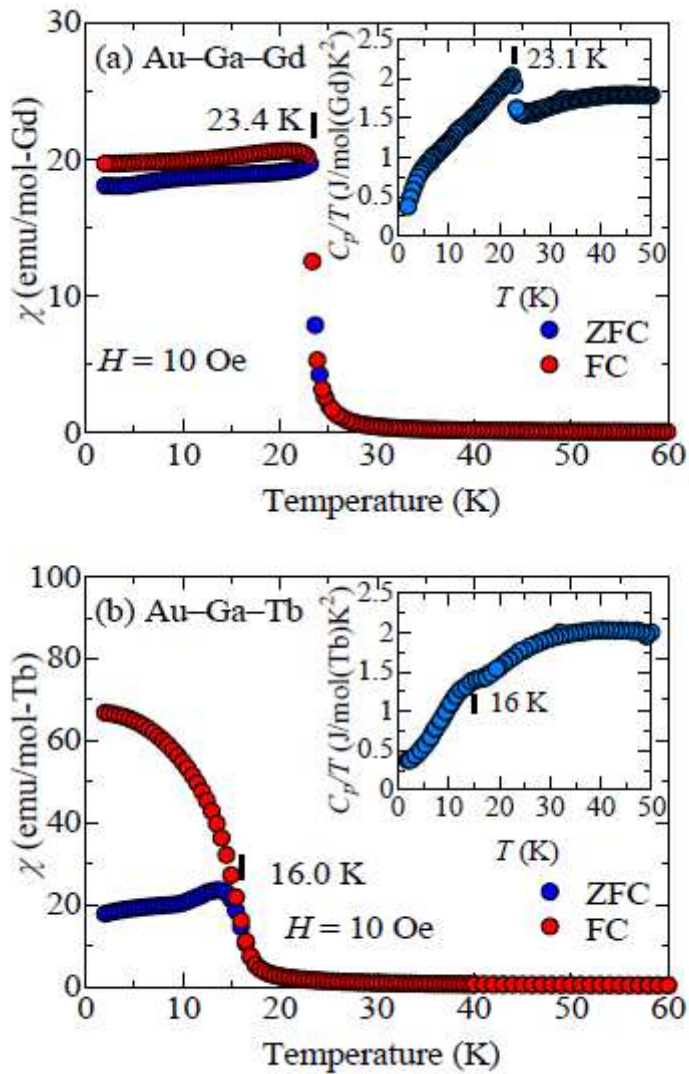


Figure 3

Temperature dependences of the FC and ZFC magnetic susceptibilities, $\chi = M/H$, for (a) the Au₆₅Ga₂₀Gd₁₅ and (b) Au₆₅Ga₂₀Tb₁₅ i QCs. FC and ZFC magnetic susceptibilities measured under 10 Oe are shown in the temperature range of 2–60 K. The insets show temperature dependences of specific heat, C_p , for Au₆₅Ga₂₀R₁₅ (R = Gd, Tb) i QCs, respectively. For the Au₆₅Ga₂₀Gd₁₅ i QC, a λ -shaped anomaly is observed at 23.1 K, clearly indicating a magnetic-transition occurrence, whereas a broad anomaly is observed around 16 K for the Au₆₅Ga₂₀Tb₁₅ i QC, suggesting the occurrence of a magnetic transition. In the inset of b, the Curie temperature T_C is estimated from the peak position of the dC_p/dT curve.

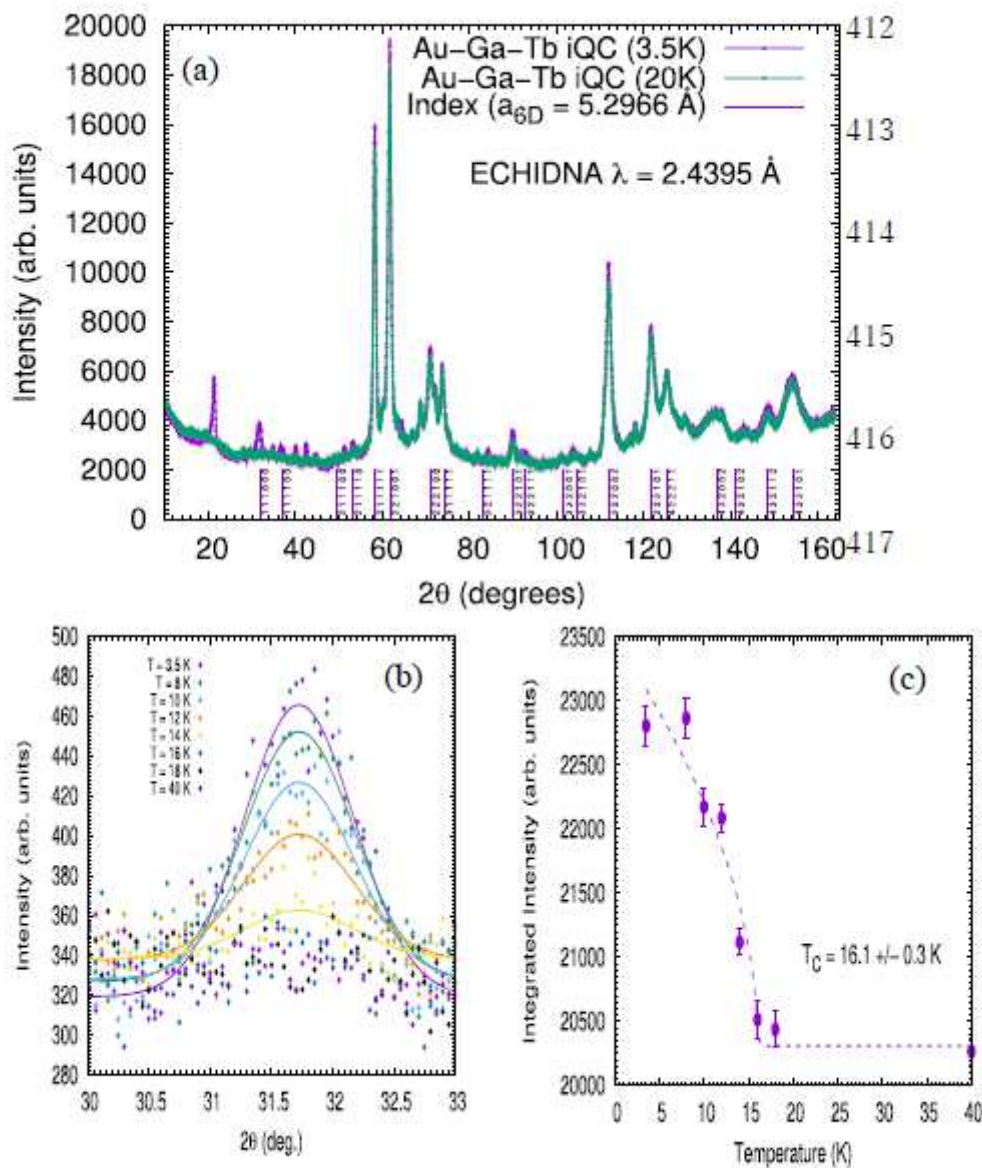


Figure 4

(a,b,c) Powder-neutron-diffraction patterns of the Au₆₅Ga₂₀Tb₁₅ i QC. In a, neutron-diffraction patterns measured at the base temperature (3.5 K) and the paramagnetic temperature (20 K), which are below and above $T_C = 16 \text{ K}$ inferred from the bulk measurements, are shown, together with the nuclear peak positions and their 6D indices for the i QC calculated with the 6D lattice constant $a_{6D} = 5.2966 \text{ \AA}$. The low- 2θ region, which contains the strongest magnetic peak from the i QC, is magnified in b. Magnetic 111000 peak is clearly observed at $2\theta = 31.8$ below T_C and disappears above T_C , evidencing the formation of long-range magnetic order in the Au₆₅Ga₂₀Tb₁₅ i QC. The temperature dependence of the integrated intensity of the 111000 reflection is plotted in c, in which the critical exponent fit $[I \propto (1 - T/T_C)^{2\beta}]$ gives an estimate of the transition temperature as $T_C = 16.1(3) \text{ K}$.

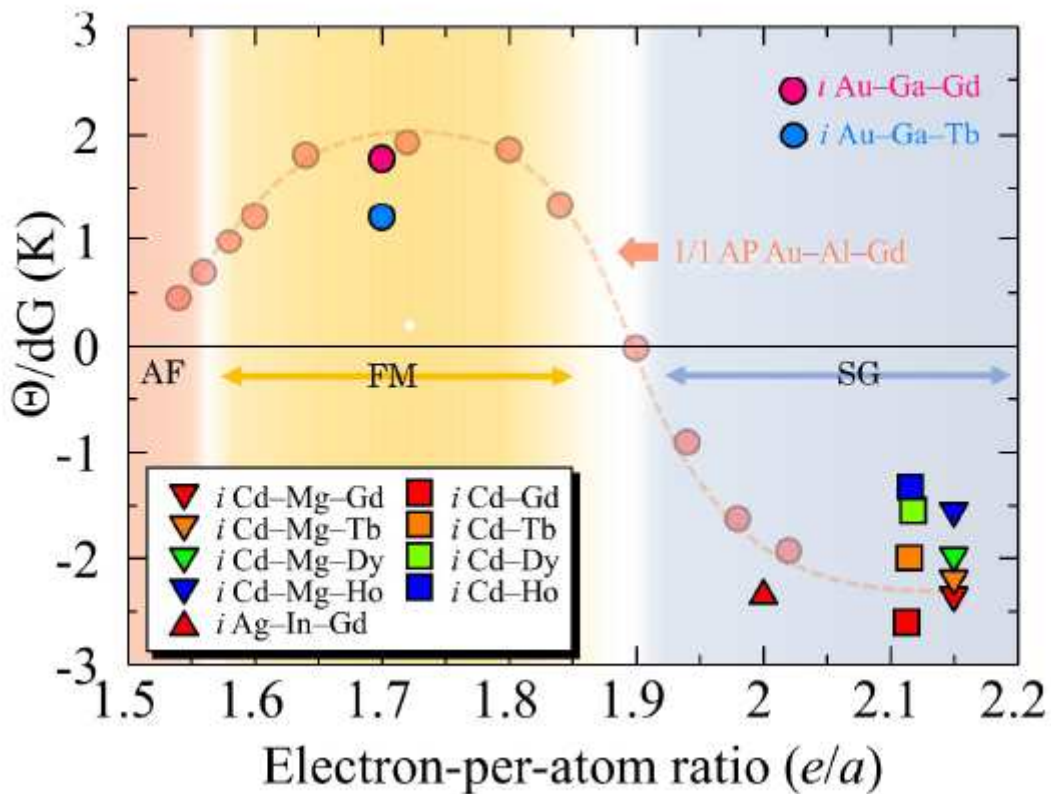


Figure 5

Normalised Weiss temperature, Θ/dG , and the magnetic ground state as a function of the e/a ratio. The Θ/dG values are plotted over a wide e/a range between 1.5 and 2.2 for all the R-containing Tsai-type i QCs reported to date, together with the Θ/dG values reported for the Au–Al–Gd 1/1 AC (orange circles) for comparison. The magnetic ground state of the Au–Al–Gd 1/1 AC is also shown. The Θ/dG values of the present Au–Ga–R (R = Gd, Tb) i QCs are large positive values, whereas those for the previously reported i QCs are large negative values without exception. This dependence of the Θ/dG value on the e/a ratio is in good agreement with the behaviour observed in the Au–Al–Gd 1/1 AC.

Supplementary Files

This is a list of supplementary files associated with this preprint. Click to download.

- [SupplementaryInformationtamuranature.pdf](#)